

Core and grain boundary sensitivity of tungsten-oxide sensor devices by molecular beam assisted particle deposition

T. P. Huelser and A. Lorke

Department of Physics and CeNIDE, University of Duisburg-Essen, Duisburg, Germany

P. Ifeacho, H. Wiggers,^{a)} and C. Schulz

Institute for Combustion and Gas Dynamics and CeNIDE, University of Duisburg-Essen, Duisburg, Germany

(Received 5 July 2007; accepted 1 October 2007; published online 20 December 2007)

In this study, we investigate the synthesis of WO_3 and WO_x ($2.6 \geq x \geq 2.8$) by adding different concentrations of tungsten hexafluoride (WF_6) into a $\text{H}_2/\text{O}_2/\text{Ar}$ premixed flame within a low-pressure reactor equipped with a particle-mass spectrometer (PMS). The PMS results show that mean particle diameters d_p between 5 and 9 nm of the as-synthesized metal-oxides can be obtained by varying the residence time and precursor concentration in the reactor. This result is further validated by N_2 adsorption measurements on the particle surface, which yielded a $91 \text{ m}^2/\text{g}$ surface area, corresponding to a spherical particle diameter of 9 nm (Brunauer-Emmett-Teller technique). H_2/O_2 ratios of 1.6 and 0.63 are selected to influence the stoichiometry of the powders, resulting in blue-colored WO_x and white WO_3 respectively. X-ray diffraction (XRD) analysis of the as-synthesized materials indicates that the powders are mostly amorphous, and the observed broad reflexes can be attributed to the orthorhombic structure of $\beta\text{-WO}_3$. Thermal annealing at 973 K for 3 h in air resulted in crystalline WO_3 comprised of both monoclinic and orthorhombic phases. The transmission electron microscope micrograph analysis shows that the particles exhibit spherical morphology with some degree of agglomeration. Impedance spectroscopy is used for the electrical characterization of tungsten-oxide thin films with a thickness of 50 nm. Furthermore, the temperature-dependent gas-sensing properties of the material deposited on interdigital capacitors are investigated. Sensitivity experiments reveal two contributions to the overall sensitivity, which result from the surface and the core of each particle. © 2007 American Institute of Physics.

[DOI: [10.1063/1.2817612](https://doi.org/10.1063/1.2817612)]

I. INTRODUCTION

Solid-state gas sensors have a huge potential for monitoring air pollutant emission in comparison to expensive gas analyzers. This is due to their unique advantages of low cost, small size, fast response time, and long operating life span. These properties provide the opportunity to use gas sensors in environmental and safety control of toxic gases, as well as in the control of combustion processes.¹⁻³ Solid-state gas sensors are based on the principle that their electrical properties change in the presence of different gaseous environments. It has been discovered that the adsorption of atoms and molecules on inorganic semiconductor surfaces can affect surface properties such as conductivity and surface potential. Hence, the composition of the ambient atmosphere affects the electrical conductance of semiconductors. These results have been applied to gas detection through the development of the first chemo-resistive semiconductor gas sensors.⁴

Semiconductor metal-oxides such as TiO_2 , SnO_2 , WO_3 , and In_2O_3 have been identified as suitable materials for gas-sensing applications.⁵⁻⁸ However, some of these materials have the disadvantages of poor selectivity, cross sensitivity, and influence of humidity. Among the above-mentioned

metal oxide, SnO_2 has attracted the greatest attention for gas-sensing applications. This is because of its native *n*-type semiconductor behavior, which allows easy interaction of the material with reactive gases. This interaction leads to a large increase or decrease of the conductivity in different environments; however, SnO_2 has been reported to exhibit poor selectivity. Therefore, alternative materials are required, which could be complementary to SnO_2 , or possess unique properties for diverse gas-sensing applications.

Tungsten oxide is known to be a very promising candidate with a good selectivity for sensing of the air pollutants NO/NO_2 , CO/CO_2 , and ethanol.⁹⁻¹¹ Furthermore, humidity-insensitive gas sensors, which have overcome some of the major disadvantages of conventional metal-oxide gas sensors, have been developed based on tungsten oxides.¹² Therefore, the creation of a gas sensor with very distinctive parameters is necessary, to obtain physic-chemical information about the electrical conduction processes of tungsten oxides using ac analysis.

The sensing behavior of bulk WO_3 is known to be a function of its chemical and physical properties such as surface area, crystallinity, stoichiometry, and phase composition. Additionally, it is accepted that the sensitivity is mainly influenced by physic-chemical reactions on the surface of the sensing material. Especially, nanoparticle-based thin-film sensors exhibit promising application properties due to the

^{a)}Electronic mail: hartmut.wiggers@uni-due.de.

large surface-to-volume ratio of each particle. Therefore, using nanoparticle thin films for sensing applications is a promising method to improve the response time and the sensitivity. Both properties are consequently influenced by the synthesis method employed for generating WO_3 particles and thin films. Some of the methods which have been employed for the synthesis of WO_3 nanoparticles and thin films include sol-gel, rf sputtering, and various precipitation techniques.¹³⁻¹⁵ While these methods have successfully yielded crystalline WO_3 nanoparticle and films, they are often constrained by multiple operation stages, or low product yield. Hence, a synthesis route that ensures both sizable quantities of products for *ex situ* analysis and materials with well-defined properties is required.

In the past few years, premixed-flame synthesis of metal-oxide nanoparticles has been successfully implemented.¹⁶⁻¹⁹ This method offers the unique advantage of chemically pure materials, short reaction time, cost effectiveness, and scale-up possibilities in comparison to the methods mentioned above. In this study, a premixed $\text{H}_2/\text{O}_2/\text{Ar}$ flat flame with dilute concentrations of WF_6 as a precursor material, operated in a low-pressure reactor, is used for the synthesis of nanosized tungsten-oxide particles. Operating the flame in a low-pressure environment provides an additional parameter (pressure), which can be used to tune the properties of the nanoparticles. Furthermore, residence time for particle growth can be varied during synthesis, while the corresponding change in mean particle diameter can be analyzed *in situ* with a particle-mass spectrometer (PMS).

One objective of this investigation has been to synthesize high surface area tungsten-oxide nanoparticles and deposit the particles on interdigital capacitors with the molecular beam assisted deposition process using the PMS. A further objective has been the characterization of the properties of the synthesized oxides, with respect to potential application in single-metal-oxide gas sensors, or combinational gas sensor devices.

II. EXPERIMENT

A. Setup

A premixed low-pressure $\text{H}_2/\text{O}_2/\text{Ar}$ flat flame stabilized on a sintered-bronze burner head is used for the synthesis of the tungsten-oxide nanoparticles by feeding the flame with low concentrations of tungsten hexafluoride vapor. The experimental setup has been previously described and reported elsewhere.²⁰

The low-pressure reactor is coupled to a particle-mass spectrometer (PMS) and the complete experimental setup is divided into three major segments that operate at different pressures. The first segment is the combustion chamber which houses the horizontally mounted, water-cooled burner head where the premixed $\text{H}_2/\text{O}_2/\text{Ar}$ flame is stabilized. It is connected to a first high-vacuum chamber via a sampling orifice, followed by a second high-vacuum chamber connected via a skimmer. The burner head can be moved in the horizontal direction, which enables the variation of the distance between the burner head and a sampling orifice. This

distance, known as the “flow coordinate,” is proportional to the residence time available for particle formation and growth. The reactor pressure p_D is kept constant at 30 mbar with the aid of a PID pressure controller. The inlet gas velocity (v_u) is maintained at 1.32 ms^{-1} , while the flow coordinate is varied between 150 and 200 mm.

The second segment is the expansion zone, which is operated at 10^{-4} mbar, and connected to the combustion zone through a 0.5 mm sampling orifice. In this segment, the particle-laden gas is supersonically expanded, causing a rapid decrease of gas temperature and density. Due to the rapid change of the flow from continuum to free-molecular conditions, all chemical and physical processes stop immediately, forming a frozen sample of the combustion aerosol.

The center of the supersonic free jet is extracted by a 0.7 mm skimmer and forms a particle-laden molecular beam inside the third segment of the interconnected vacuum chambers operated at 10^{-6} mbar. In this segment, particle-mass analysis, which is later converted to particle size distribution, is performed using the PMS. The design, test, and application of the PMS to size analysis of nanoscale particles have been reported in Ref. 21.

A mixture of 1% tungsten hexafluoride (WF_6) in argon is prepared in a mixing vessel by a partial pressure method.²² The diluted WF_6 is fed into the flame reactor via a steel pipe using a mass-flow controller. Upon entering the flame, the diluted WF_6 is thermally dissociated, followed by an exothermic gas-phase reaction that generates a gas phase of supersaturated metal oxides. At lower temperatures downstream of the flame, condensation of metal-oxide vapor leads to the formation of primary particles which further grow into agglomerates and aggregates by coalescence and coagulation.²³ The synthesized particles are thermophoretically sampled on a water-cooled plate located inside the combustion chamber next to the sampling orifice. Furthermore, particles can be sampled on transmission electron microscope (TEM) grids at the same position, using a pneumatic sampling device by rapid insertion and withdrawal in the particle-laden gas from the combustion segment.

Within the third chamber the molecular beam that contains charged and uncharged particles is directed through an electric field between two parallel arranged electrodes. The electric field between the electrodes separates the charged particles according to their polarity and splits the well-focused beam into a fan of charged particles. Particles with low kinetic energy show a stronger deflection than those with high kinetic energy. The relation between the deflection voltage U_c and the kinetic energy of the charged particles is

$$U_c = \text{const.} \frac{m_p v_p^2}{ze^2}, \quad (1)$$

where m_p is the particle-mass, v_p the velocity of particles in the beam, and z the number of elementary charges, respectively. Based on Fuchs' theory, each particle can be assumed to be singly charged. The current generated by these charges can be measured using a Faraday cup and converted into a particle current I_p .

From the principles of the PMS it is also clear that the current I_p is not directly proportional to the probability den-

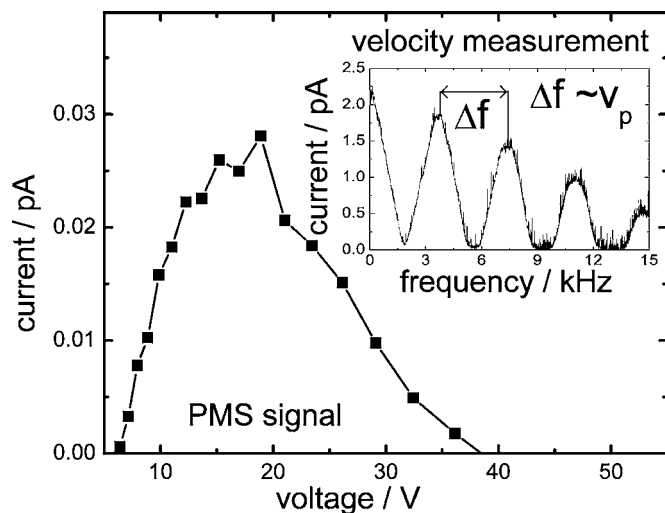


FIG. 1. A typical PMS signal: measured current vs deflection voltage. The inset shows a velocity measurement at a fixed deflection voltage.

sity function (PDF) of the particle mass or the particle kinetic energy. Roth and Hospital²¹ have shown that the following relation between the measured particle current versus deflection voltage U_c and the PDF holds:

$$\text{PDF}(m_p) = \text{const.} \frac{I_p(U_c)}{U_c}. \quad (2)$$

The setup allows for the determination of the velocity of the charged particles in the beam. By tuning the pulse frequency of two repelling potentials with a spatial distance and perpendicular to the molecular beam this device operates as a velocity filter. The resulting current plotted as a function of pulse frequency shows distinct maxima and minima, which in turn can be related to the particle velocity. The value of v_p satisfies the following equation:

$$v_p = 2f_{\min}l_g. \quad (3)$$

Due to the difficulty associated with identifying the first frequency minimum, which corresponds to a packet length l_g , it is more practicable to work with the difference between two minima, whereby $\Delta f = 2f_{\min}$. Hence, Eq. (3) becomes

$$v_p = \Delta f_{\min}l_g. \quad (4)$$

In this equation, Δf is the frequency difference between two current maxima. A typical PMS signal (current/voltage) is shown in Fig. 1.

With the PMS signal, the velocity measurement, and the bulk density of the material, the PDF of the particle diameter can be obtained from the measured data (Fig. 1). The mean particle diameter d_p as well as the geometric standard deviation σ_g can thus be obtained from Fig. 2.

B. Sensing mechanism

The sensing mechanism of nanoparticles with respect to CO and NO measurements is attributed to interactions between different species on the particle surface. It has been established that both gases react with preadsorbed oxygen or oxygen from the lattice, and release electrons into the conduction band. The dependence of conductivity on the CO or

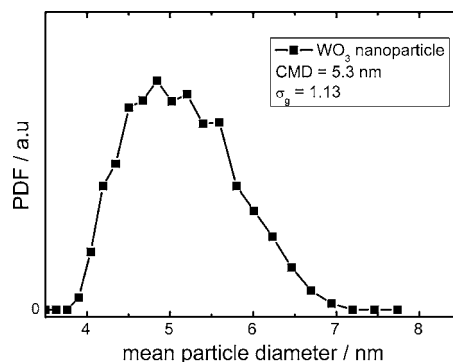


FIG. 2. Particle diameter distribution obtained from the data shown in Fig. 1.

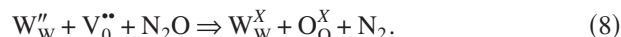
NO ratio in the atmosphere is described in a model by Morrison²⁴ and also related to temperature by Reyes *et al.*²⁵ A visualization of the adsorption sites of oxygen on WO_3 nanoparticles is given by Ottaviano *et al.*²⁶ The reducing chemical surface reactions of NO and CO with the WO_3 particles are displayed in Eqs. (5) and (6) in Kröger-Vink notation,



Additionally, the disproportionation of NO at the particle surface takes place as shown in Eq. (7),



Therefore, further oxidizing reactions following Eq. (8) occur,



III. RESULTS AND DISCUSSION

A. PMS and TEM image analysis

Figure 3 shows the PMS analysis of WO_3 nanoparticles for flow coordinates between 150 and 200 mm. The measured mean particle diameter d_p ranges between 5 and 9 nm, while the geometric standard deviation σ_g varies between 1.07 and 1.19. With increasing flow coordinate, both, d_p and σ_g increase.

The sampling of the particles is achieved by positioning the burner head at a flow coordinate of 170 mm. As men-

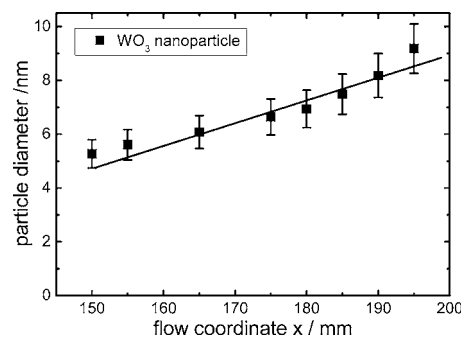


FIG. 3. Mean particle diameter as a function of flow coordinate.

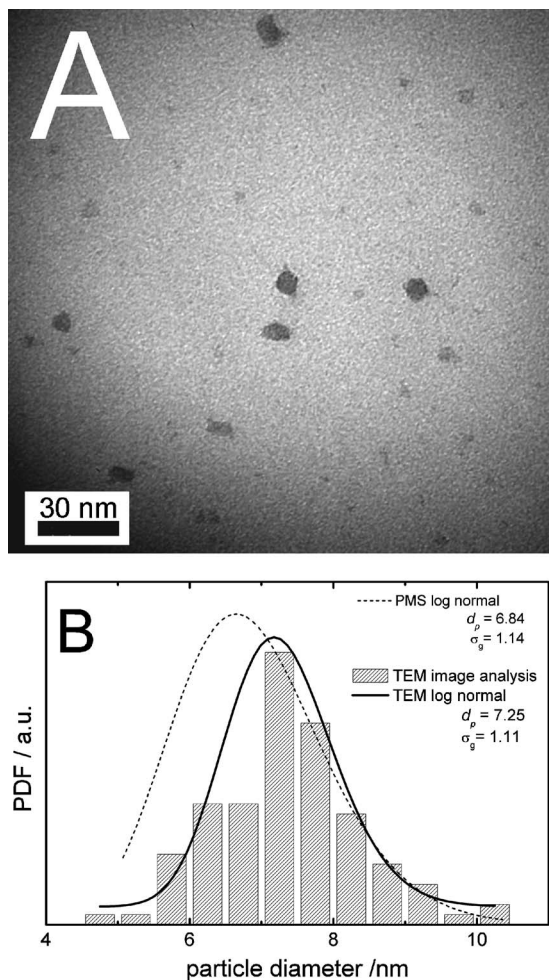


FIG. 4. (a) TEM micrograph of WO_3 nanoparticles; (b) Comparative analysis of particle size distribution from TEM image analysis and PMS.

tioned before, a pneumatic TEM sampling device is used for thermophoretic deposition of particles on TEM grids. The position for the TEM sampling corresponds to the position of the sampling orifice, where a sample aerosol is extracted for PMS analysis. Figure 4(a) shows a TEM image of the tungsten-oxide nanoparticles on a carbon layer of the TEM grid. The results of the particle size distribution obtained from PMS and TEM image analysis can thus be compared as shown in Fig. 4(b).

The TEM image shows that the WO_3 particles have a roughly spherical morphology. However, some degree of agglomeration is observed, which is typical for high-temperature gas-condensation processes. Three hundred individual particles are selected from micrographs, from which classes and probabilities are determined. Mean particle diameters of $d_p = 6.84$ and 7.25 nm corresponding to TEM image analysis and PMS, respectively, are obtained. The results are in good agreement with the slight disparity attributed to measurement errors. The geometric standard deviation σ_g is 1.11 and 1.14 from TEM and PMS, respectively.

The ability to control, characterize, and sample nanomaterials during synthesis operations provides the basis for size-selected deposition of the metal oxide from the molecular beam on substrates for *ex situ* analysis.

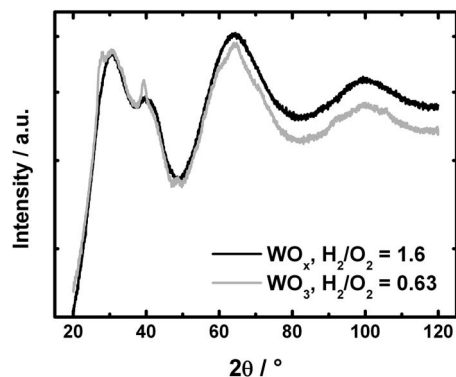


FIG. 5. XRD diffractogram of as-synthesized tungsten-oxide nanoparticles generated with different H_2/O_2 ratios.

B. XRD

WO_3 nanoparticles are synthesized with two different H_2/O_2 ratios of 0.625 and 1.6, which represent lean (excess oxygen) and rich conditions. The essence of this investigation is to determine if nonstoichiometric WO_x nanoparticles can be generated in oxygen deficient conditions. The reactor pressure and inlet gas velocity are kept constant at 30 mbar and 1.32 m/s, respectively, for both experimental investigations, while the precursor concentration is maintained at 500 ppm. For the low oxygen concentration a blue-colored powder is obtained, while a white-colored powder is generated for higher oxygen concentration. Blue-colored tungsten-oxide particles have been reported to occur either during oxygen deficient synthesis or during thermal annealing in a reducing atmosphere.²⁶ As a result, oxygen defects occur, which results in a nonstoichiometric tungsten oxide WO_x , whereby $2 < x < 3$. In contrast, the white-colored tungsten oxide is assumed to be fully oxidized WO_3 nanoparticles. In order to validate this assumption and investigate any difference, x-ray diffraction measurements on the particles are performed.

The x-ray diffraction (XRD) pattern is detected with a highly sensitive semiconductor detector (X'Celerator/Panalytical) equipped with a cobalt x-ray source and an iron filter to suppress any k_β -radiation. From the XRD spectrum of as-synthesized tungsten-oxide nanoparticles shown in Fig. 5, both particles show a similar spectrum with broad reflexes which could not be matched to any known polymorph of tungsten oxide. The broad reflexes indicate that, despite the high amorphous nature of the materials, some degree of ordered arrangement exists in the crystal lattice of the materials.

It has been reported that tungsten oxide can crystallize into several polymorphs when exposed to high temperatures.²⁷ Hence, in order to confirm that the as-synthesized materials are tungsten oxide, the materials are thermally annealed at 700°C for 10 min in air. The thermally annealed particles are consequently analyzed with XRD and the diffractogram is presented in Fig. 6. The sharp reflexes seen on the diffractogram indicate that a transformation to a highly ordered crystallite has occurred in the material. The reflexes are matched to monoclinic $\gamma\text{-WO}_3$ nano-

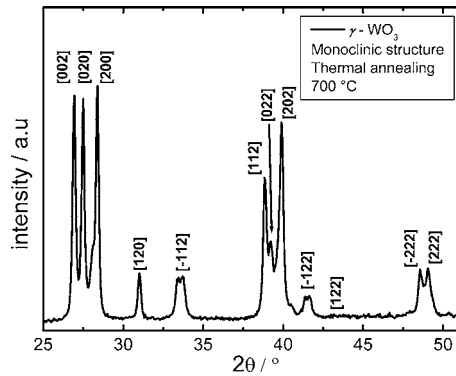


FIG. 6. XRD diffractogram of tungsten oxide thermally annealed at 700 °C for 10 min in air.

particles with the $P2_1/n$ space group. This result confirms the successful synthesis of tungsten-oxide nanoparticles in the low-pressure flame reactor.

The sensing properties of both tungsten-oxide powders deposited on interdigital capacitors (IDC) substrate are performed in order to establish the suitability and sensitivity of both powders for gas sensing devices.

C. Sensor geometry

The sensor is realized by depositing the tungsten-oxide nanoparticles on top of an interdigital capacitor realized on a p -type silicon wafer with an insulating SiO_2 layer on top. An array of interdigitated gold contacts is arranged using electron beam lithography.

Figure 7 shows a scanning electron microscope image of the sensor structure with the deposited WO_3 nanoparticles. The enlargement in the inset in Fig. 7 shows the nanoparticle thin film on the interdigitated structure. The device is achieved by placing the sensor along the path of the particle-laden molecular beam, which arises from the pressure difference in the various segments of the reactor. Assuming a closed arrangement of the particles with a filling factor of 87%, a film thickness of about 50 nm is calculated.

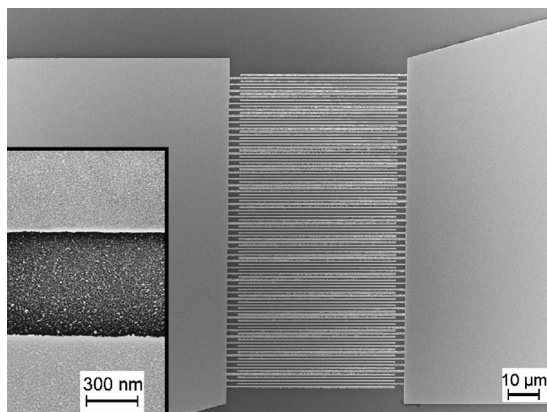


FIG. 7. SEM image of an interdigital capacitor with gold "fingers" and electrodes on a p -doped silicon substrate with a 1000 nm SiO_2 top layer; inset shows a close-up which resolves the nanoparticle thin film on top.

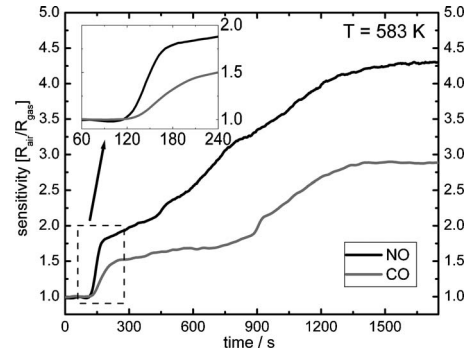


FIG. 8. Sensitivity of WO_3 nanoparticles on interdigital transducers against time for measurements under synthetic air with 1000 ppm reactive gases. The inset shows a magnification of the dashed box. The reactive gas is added after 120 s.

D. Electrical measurement

To perform ac measurements under the influence of reactive gases, the sample is kept in a glass tube with a gas inlet and outlet at the ends of the tube. The inlet is connected to a gas-mixing system as previously described by Rakesh *et al.*²⁸ The measurement cell is encased by a temperature-controlled tube furnace to vary the temperature of the sample in the range between 553 and 583 K, after annealing the sample at 583 K for several hours. Impedance spectroscopy (IS) measurements are performed under synthetic air, synthetic air with 1000 ppm CO, and synthetic air with 1000 ppm NO in steps of 10 K down to 553 K. After each measurement series the sample is annealed again at 583 K under synthetic air.

For impedance measurements, a Solatron SI 1255 frequency response analyzer (FRA) in combination with a dielectric interface SI 1296 is used in the frequency range between 1 Hz and 1 MHz with 17 points per decade. The control of the FRA, the data recording, and the temperature adjustment are realized with a computer. Before measuring the impedance of the material, the sample is annealed at 583 K under a gas flow of 100 sccm synthetic air for several hours. For a quantitative analysis of our measurements, the data have been fitted using adequate equivalent circuit by means of a nonlinear least-square fit algorithm.

1. Sensitivity

To investigate the sensitivity of the particulate tungsten-oxide thin films, the change of resistance R under synthetic air with reactive gas species CO and NO is measured at 583 K after annealing for several hours under synthetic air. For this purpose the impedance data at a frequency of 100 Hz (which is still in the dc range) are recorded as a function of time for a 30 min time period.

Figure 8 shows the normalized sensitivity $S=R_{\text{air}}/R_{\text{gas}}$ for 1000 ppm NO and 1000 ppm CO in synthetic air. In both cases the reactive gas has been added after a runtime of 120 s. Both, the CO and NO data exhibit an increase of sensitivity during the measurements and a leveling off at about $t=1500$ s. At this time, a sensitivity $S=4.3$ for NO and $S=2.9$ for CO is observed. For both gases the increase of conductivity can be explained by the injection of electrons.

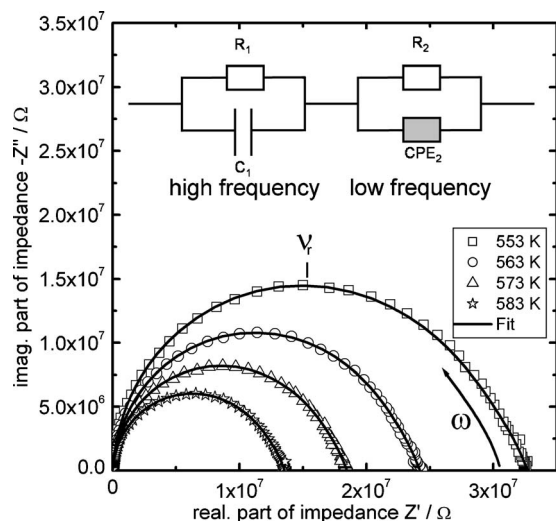


FIG. 9. Impedance data in Nyquist representation for different temperatures under synthetic air with 1000 ppm CO. ν_r represents the resonance frequency of the high frequency contribution for the measurement at 553 K. The equivalent circuit in the upper part is used to analyze the data, while the lines represent the result of our fits.

However, the data reveal a faster increase of sensitivity for NO as well as a better sensitivity. Furthermore, we observe a similar time dependence for both species within the first 120 s after the addition of the gases, followed by a slower, but dominant, increase of sensitivity during longer exposure. This fast change in sensitivity during the first seconds usually is not seen with common WO_3 sensors and can be attributed to the high surface-to-volume ratio of the nanosized oxide. To further substantiate this, impedance spectra have been measured to investigate core and grain boundary sensitivity in detail.

2. Impedance data

The results received from the sensitivity measurements reveal stable saturation values before the reactive gases are added, as well as 1500 s after adding the gases. Therefore, it is possible to perform time-consuming impedance spectroscopy under such stable conditions. For the impedance measurements the same sample conditioning is used as for measuring the sensitivity of WO_3 thin films. After annealing and stabilizing with 1000 ppm NO and 1000 ppm CO, impedance data are recorded from 583 to 553 K in 10 K steps.

Figure 9 shows the Nyquist diagram of the impedance measurements in the temperature range between 553 and 583 K under CO exposure. The decrease of resistance with increasing temperature is a well-known property of semiconducting materials. All measurements exhibit an almost-perfect quarter of a circle for frequencies higher than the resonance frequency ν_r (apex of the circle). This can be ascribed to a very narrow relaxation time distribution due to the fact that the sensor material consists of nearly monodisperse WO_3 particles. For frequencies lower than the resonance frequency (right-hand side of the spectra) the measured spectra do not deviate from a semicircle, but show a widening toward higher impedances. Similar results are obtained for granular tungsten oxide by Ling *et al.*,²⁹ and for

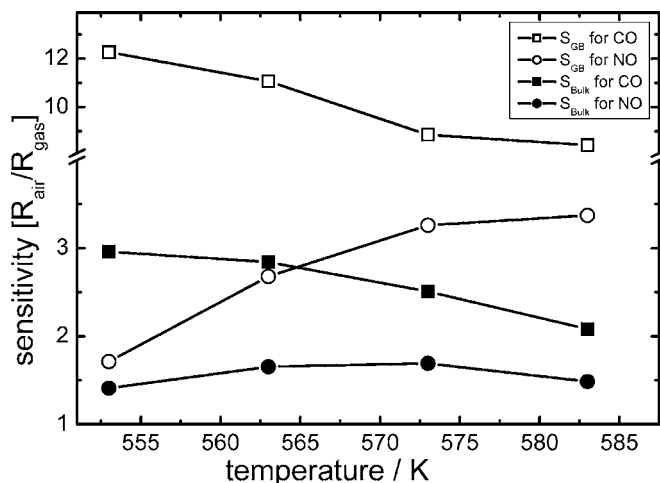


FIG. 10. Core and grain boundary sensitivities of tungsten-oxide nanoparticles on CO and NO against temperature. The squares represent the sensitivity of CO and the circles those of NO, respectively.

solid thin films by Labidi *et al.*³⁰ This behavior consequently indicates a second scattering process at low frequencies and has been described in detail by Barsan *et al.*³¹

To perform the NLLS (nonlinear least-square) fits, an equivalent circuit of two serial elements has been used consisting of one RC element describing the high-frequency (HF) region and a second one, containing a so-called “constant phase element”³² and a resistor, which accounts for the low-frequency (LF) region. The high-frequency signal originates from the semiconducting core of each particle (bulk), while the low-frequency contribution originates from the intergranular contacts of the particles (grain boundary). As can be seen from Fig. 9, measured data and model calculations match perfectly. The resistances obtained from the fit results have been used to determine the different contributions (bulk and grain boundary) to the overall sensitivities on NO and CO. Figure 10 shows the grain boundary (S_{GB}) and the bulk S_{bulk} sensitivities calculated from the fit results.

The data of the separated sensitivities are in good agreement with the overall sensing results (see Fig. 8). From Fig. 10 it is obvious that the sensitivity for CO is significantly higher compared to NO at temperatures < 570 K, while this behavior turns above 570 K. Furthermore, in all cases the sensitivity of the grain boundary is enhanced compared to that of the bulk.

Infrared studies on NO adsorption on $\text{W}/\text{Al}_2\text{O}_3$ catalysis have shown that NO, contrary to CO, favors adsorption in twin form on the catalysis surface, and different nitrogen oxides like N_2O , N_2O_3 , and NO_2 are observed.^{33,34} Weingand *et al.* reported that the stable species produced after coadsorption of NO and O_2 on WO_3/ZrO_2 surfaces are NO^+ and nitrates (NO_3^-).³⁵ Thus, the infrared studies suggest that the adsorption/desorption and surface chemistry of NO is quite complex compared to CO. Moreover, it is generally accepted that NO interacts more strongly with transition metals than CO. As a result, the adsorption of CO and desorption of CO_2 is expected to occur at lower temperatures compared to NO/NO_2 .

The results of the ac measurements at 583 K are in good agreement with those derived from the dc measurements at the same temperature. Nevertheless, the overall sensitivity $S_{\text{overall}} = (R_1 + R_2)_{\text{air}} / (R_1 + R_2)_{\text{gas}}$ is dominated by the contribution of the core (R_1) and only slightly affected by the grain boundary effects (R_2). For this reason, we attribute the instantaneous increase in sensitivity (see Fig. 8) directly after adding the reactive gases to a fast surface reaction at the grain boundaries followed by a slowly rising sensitivity due to a change in bulk conductivity.

IV. CONCLUSION

Nanosized WO_3 particles are successfully synthesized in a low-pressure $\text{H}_2/\text{O}_2/\text{Ar}$ premixed flame using dilute concentrations of tungsten hexafluoride (WF_6). The mean particle diameter of the as-synthesized material is controlled between 5 and 9 nm by varying the residence time for particle growth in the reactor as a function of the flow coordinate. Furthermore, the geometric standard deviation for particles produced at the beginning of the formation process is nearly monodisperse ($\sigma_g < 1.11$), and reaches values above 1.3 at higher coordinates. The as-synthesized WO_3 nanoparticles have a high amorphous content with some degree of the orthorhombic crystal structure, as indicated by relatively broad reflexes in the x-ray diffraction pattern. For low oxygen concentrations, nonstoichiometric (blue-colored) WO_x particles are generated. This material shows no significant difference in crystal structure in comparison to stoichiometric WO_3 nanoparticles. The particles are deposited on a sensor structure by molecular beam assisted particle deposition and the sensing properties are electrically characterized in synthetic air and in the presence of 1000 ppm of CO and NO, respectively. Impedance spectroscopy reveals good sensitivities of the tungsten-oxide nanoparticle thin film. The sensor exhibits different sensitivities to the investigated reactive gas species NO and CO. It is established that the overall sensitivity mainly consists of two different contributions as determined by impedance spectroscopy results. Our studies show that the surface sensitivity is much higher than the sensitivity of the core material. In addition, it is observed that the optimum temperature for sensing CO is lower than that for NO. We attribute this fact to the different surface chemistry and adsorption/desorption behavior of the two gas species. Therefore, nanosized tungsten oxide with a particle diameter smaller than 7 nm seems to be a very good candidate for a fast detection of air pollutants originating from combustion processes.

ACKNOWLEDGMENTS

Financial support from SFB 445 and technical support by "Center for Nano Integration Duisburg-Essen" (CeNIDE)

is gratefully acknowledged. The authors would also like to thank Dr. Rakesh Joshi and Dr. Einar Kruis for providing the measurement setup for the sensing measurements and their experimental knowledge.

- ¹O. Pummakarnchana, N. Tripathi, and J. Dutta, *Sci. Technol. Adv. Mater.* **6**, 251 (2005).
- ²D.-D. Lee and D.-S. Lee, *IEEE Sens. J.* **1**, 214 (2001).
- ³M. A. Martin, J. P. Santos, A. H. Vasquez, and J. A. De Agapito, *Electron Technol.* **33**, 292 (2000).
- ⁴P. T. Ivanov, Ph.D. thesis, University Rovira i Virgili, 2004.
- ⁵J. Tamaki, T. Hayashi, Y. Yamamoto, and M. Matsuoka, *Electrochemistry (Tokyo, Jpn.)* **71**, 468 (2003).
- ⁶Y. Shimizu, A. Kawasoe, Y. Takao, and E. Makoto, *Proc.-Electrochem. Soc.* **96**, 117 (1997).
- ⁷C. A. Papadopoulos, D. S. Vlachos, and J. N. Avaritsiotis, *Sens. Actuators B* **32**, 61 (1996).
- ⁸G. Lu, N. Miura, and N. Yamazoe, *Sens. Actuators B* **35**, 130 (1996).
- ⁹A. Ponzoni, E. Comini, M. Ferroni, and G. Sberveglieri, *Thin Solid Films* **490**, 81 (2005).
- ¹⁰G. Sberveglieri, L. Depero, S. Groppelli, and P. Nelli, *Sens. Actuators B* **26**, 89 (1995).
- ¹¹F. Ahmed, S. Nicoletti, S. Zampolli, I. Elmi, A. Parisini, L. Dori, A. Mezzi, and S. Kaciulis, "Sensors and Microsystems," in *Proceedings of the 7th Italian Conference, Bologna, Italy, 4–6 February 2002* (2002), pp. 197–204.
- ¹²M. Sriyudthsak and S. Supothina, *Sens. Actuators B* **113**, 265 (2006).
- ¹³S. Li, I. N. Germanenko, and M. S. El-Shall, *J. Cluster Sci.* **10**, 533 (1999).
- ¹⁴Z. Lu, S. M. Kanan, and C. P. Tripp, *J. Mater. Chem.* **12**, 983 (2002).
- ¹⁵H. G. Choi, Y. H. Jung, and D. K. Kim, *J. Am. Ceram. Soc.* **88**, 1684 (2005).
- ¹⁶P. Ifeacho, H. Wiggers, and P. Roth, *Proc. Combust. Inst.* **30**, 2577 (2005).
- ¹⁷D. Lindackers and P. Roth, *Chem.-Ing.-Tech.* **69**, 143 (1997).
- ¹⁸S. E. Pratsinis, O. Arabi-Katbi, C. M. Megaridis, P. W. Morrison, Jr., S. Tsantilis, and H. K. Kammler, *Mater. Sci. Forum* **343–346**, 511 (2000).
- ¹⁹B. Zhao, K. Uchikawa, J. C. McCormick, C. Y. Ni, J. G. Chen, and H. Wang, *Proc. Combust. Inst.* **30**, 2569 (2005).
- ²⁰C. Janzen and P. Roth, *Combust. Flame* **125**, 1150 (2001).
- ²¹P. Roth and A. Hospital, *J. Aerosol Sci.* **25**, 61 (1994).
- ²²V. Simanzhenkov, P. Ifeacho, H. Wiggers, J. Knipping, and P. Roth, *J. Nanosci. Nanotechnol.* **4**, 157 (2004).
- ²³T. T. Kostas and M. Hampden-Smith, *Aerosol Processing of Materials* (Wiley-VCH, New York, 1999), p. 266–278.
- ²⁴S. R. Morrison, *Sens. Actuators* **11**, 283 (1987).
- ²⁵L. F. Reyes, A. Hoel, S. Saukko, P. Heszler, V. Lantto, and C. G. Granquist, *Sens. Actuators B* **117**, 128 (2006).
- ²⁶L. Ottaviano, E. Maccallini, and S. Santucci, *Surf. Sci.* **492**, L700 (2001).
- ²⁷J. Gallardo, thesis, University de Barcelona, 2003.
- ²⁸R.K. Joshi and F. E. Kruis, *Appl. Phys. Lett.* **89**, 153116 (2006).
- ²⁹Z. Ling, C. Leach, and R. Freer, *J. Eur. Ceram. Soc.* **23**, 1881 (2003).
- ³⁰A. Labidi, C. Jacolin, M. Bendahan, A. Abdelghani, J. Guerin, K. Aguir, and M. Maaref, *Sens. Actuators B* **106**, 713 (2005).
- ³¹N. Bârsan and U. Weimar, *J. Phys.: Condens. Matter* **15**, R813 (2003).
- ³²E. Barsoukov and J. M. Macdonald, *Impedance Spectroscopy: Theory, Experiment, and Applications* (Wiley and Sons, Chichester, 2005).
- ³³K. Hadjiivanov, P. Lukinska, and H. Knötzinger, *Catal. Lett.* **82**, 73 (2002).
- ³⁴Y. Yan, Q. Xin, S. Jiang, and X. Guo, *J. Catal.* **131**, 234 (1991).
- ³⁵T. Weingand, S. Kuba, K. Hadjiivanov, and H. Knötzinger, *J. Catal.* **209**, 539 (2002).